catalysts

MDPI

Article

Relationship Between Number and Strength of Acid–Base Catalytic Sites and Their Performances in Isopropanol Dehydration Reaction

Georgeta Postole [1,*], Sandra Segondy [1], Tristan Cabanis [1], Tien-Hoang Nguyen [1], Aline Auroux [1] and Jean-Luc Dubois [2,*]

[1] Université Claude Bernard Lyon 1, CNRS, IRCELYON, UMR 5256, F-69100 Villeurbanne, France; tristan.cabanis@ircelyon.univ-lyon1.fr (T.C.); tien-hoang.nguyen@ircelyon.univ-lyon1.fr (T.-H.N.)
[2] Trinseo Netherlands B.V., Innovatieweg 14, 4542 NH Hoek, The Netherlands
* Correspondence: georgeta.postole@ircelyon.univ-lyon1.fr (G.P.); jdubois@trinseo.com (J.-L.D.)

Abstract

Commercial alumina and silica–alumina catalysts were investigated for propylene (PEN) production via an isopropanol (IPA) dehydration reaction between 200 and 300 °C at an atmospheric pressure and IPA partial pressure of 5136 Pa. The reaction conditions were chosen to fit with the further conversion of PEN into value-added compounds with minimal capital cost, and the conceptual process design was discussed. The textural properties, structure and chemical composition of as-received and hydrothermally treated catalysts were characterised by the adsorption–desorption of N_2, X-ray fluorescence, X-ray diffraction and Nuclear Magnetic Resonance spectroscopy. The adsorption microcalorimetry of NH_3 and SO_2 was used to determine the amount, strength and strength distribution of acid–base sites, while the nature of the acid sites was investigated by Fourier Transform Infraed spectroscopy. Surface area, pore-size distribution and pore volume were not determining factors for the catalytic performances of studied solids in the conditions used here. The best-performing catalyst combined stable textural properties and a high number of high-strength acid sites (Q_{diff} > 150 kJ/mol NH_3) under hydrothermal conditions. The importance of determining the number and strength of acid sites of water-aged catalysts, when considering reactions where water is present as reactive or product, is underlined.

Keywords: adsorption microcalorimetry; acid–base sites; Isopropanol dehydration; propylene; silica–alumina

Academic Editor: Eric M. Gaigneaux

Received: 30 June 2025
Revised: 3 August 2025
Accepted: 6 August 2025
Published: 12 August 2025

Citation: Postole, G.; Segondy, S.; Cabanis, T.; Nguyen, T.-H.; Auroux, A.; Dubois, J.-L. Relationship Between Number and Strength of Acid–Base Catalytic Sites and Their Performances in Isopropanol Dehydration Reaction. *Catalysts* **2025**, *15*, 768. https://doi.org/10.3390/catal15080768

1. Introduction

Propylene (PEN) is considered a versatile building block in most of the petrochemical industries to produce valuable chemical intermediates such as polypropylene, acrylonitrile, acrolein, acrylic acid, etc. Currently, PEN is primarily obtained as a co-product in the steam cracker of naphtha and in refineries fluid catalytic cracking (FCC) units, but also through propane dehydrogenation, methanol to propylene/olefin (MTP/MTO) processes or through metathesis reaction [1]. In a recent review, Busca et al. summarised the advantages and disadvantages of different methods used for PEN production [2].

Due to the worldwide increasing demand for propylene (about 135 million tonnes in 2025 [2–7]), as well as its shortages due to the shale gas revolution and environmental challenges, the production of propylene from alternative, economically viable, and sustainable pathways is necessary.

Isopropanol, mainly used as a solvent, is a good candidate as a raw material for PEN production through its catalytic dehydration [8]. IPA catalytic conversion is often employed by the scientific community as a test reaction to clarify the prevailing catalytic properties for many solid materials [9,10]. Indeed, catalysts can be screened according to their performances in isopropanol dehydration (to PEN or di-isopropyl ether, DIPE) or dehydrogenation (to acetone, ACE) reactions. As is widely accepted, dehydration reaction takes place on acid sites, whereas dehydrogenation is accomplished over basic or redox centres [11–14] for many catalytic systems. The acid–base properties of the materials can be thus correlated with the product type and amount. In these studies, a low isopropanol concentration in the feed stream is generally used in order to simplify the reaction mechanism and to avoid the formation of secondary products, while the measurements are (and should be) carried out below 25% conversion [12,13,15].

Isopropanol dehydration to propylene is practiced at commercial scale in very limited cases (e.g., in cumene synthesis as a consecutive reaction). However, due to the possible IPA supply from multiple sites and feedstocks [16] and the facilities in its transport and storage (liquid product with low boiling point, T_b = 83 °C), isopropanol is an interesting raw material for large-scale production of propylene. A challenge consists in avoiding the intermolecular dehydration of IPA that will lead to di-isopropyl ether and the rehydration of propylene into n-propanol. This implies catalyst optimisation, which requires properties including specific acidity and porosity, good stability, resistance to steam and high activity. Furthermore, isopropanol can be an appropriate feedstock for small production sites, which can then produce on-site and on-demand a large panel of value-added compounds, therefore avoiding their transport and storage. When the propylene production is coupled with its further transformation into value-added compounds, the capital cost can be minimised if IPA is co-fed to an oxidation reactor, as proposed by Dubois et al. [17], for the oxidative coupling of alcohols to acrolein. In this configuration, the dehydration reaction should be performed at a low contact time, at an intermediate partial pressure, over a catalyst combining both acid/base and redox functions, or layers of acid and oxidation catalysts.

This work is part of an extended study program dealing with the experimental investigation to validate the proof of concept. It focuses on the dehydration reaction as the first step of the process. In this context, this paper reports on the characterisation from a structural, textural, acid/base and catalytic point of view of commercial alumina-based solids, cost-effective materials that can be used for application at the industrial scale. Commercial samples were characterised by powder X-ray diffraction, nitrogen physisorption (BET), X-ray fluorescence, nuclear magnetic resonance spectroscopy, Fourier transform infrared spectroscopy and the adsorption microcalorimetry of NH_3 and SO_2. The catalytic dehydration of isopropanol to propylene was performed at 200, 250 and 300 °C, and an attempt was made to correlate the activity with the structure and the acid/base properties of tested powders.

2. Results and Discussion

2.1. Characterisation of Alumina-Based Catalysts

Figure 1 shows the XRD patterns of studied solids. The peak positions for alumina pure samples corresponded to gamma (2θ = 36.9°, 39.4°, 46.0° and 67.0° [18]) and theta (2θ = 31.6°, 32.8°, 37.1°, 39.9°, 45.3°, 50.9°, 60.1° and 67.5° [19]) phases with cubic and monoclinic crystal systems, respectively. Both γ and θ phases are metastable aluminas with similar face-centred cubic oxygen sublattices but cations present in various proportions in both octahedral and tetrahedral lattice sites [18]. Indeed, the γ-to-θ phase transition takes place by aluminium migration in order to reduce strong Al–Al interactions, while oxygen atoms remain fixed [20]. SiO_2-Al_2O_3 with lowest silica content exhibits diffraction peaks

corresponding to (311), (222), (400) and (440) crystal planes of the γ-Al_2O_3 cubic system. With increasing silica content in 30-SiO_2-Al_2O_3, the intensity of γ-Al_2O_3 characteristic peaks was decreased, and a new broad diffraction peak was visible at 2θ = 15–30°, attributed to amorphous silica. The peak assigned to silica phase became more pronounced in 75-SiO_2-Al_2O_3, while the characteristic peaks of alumina almost disappeared.

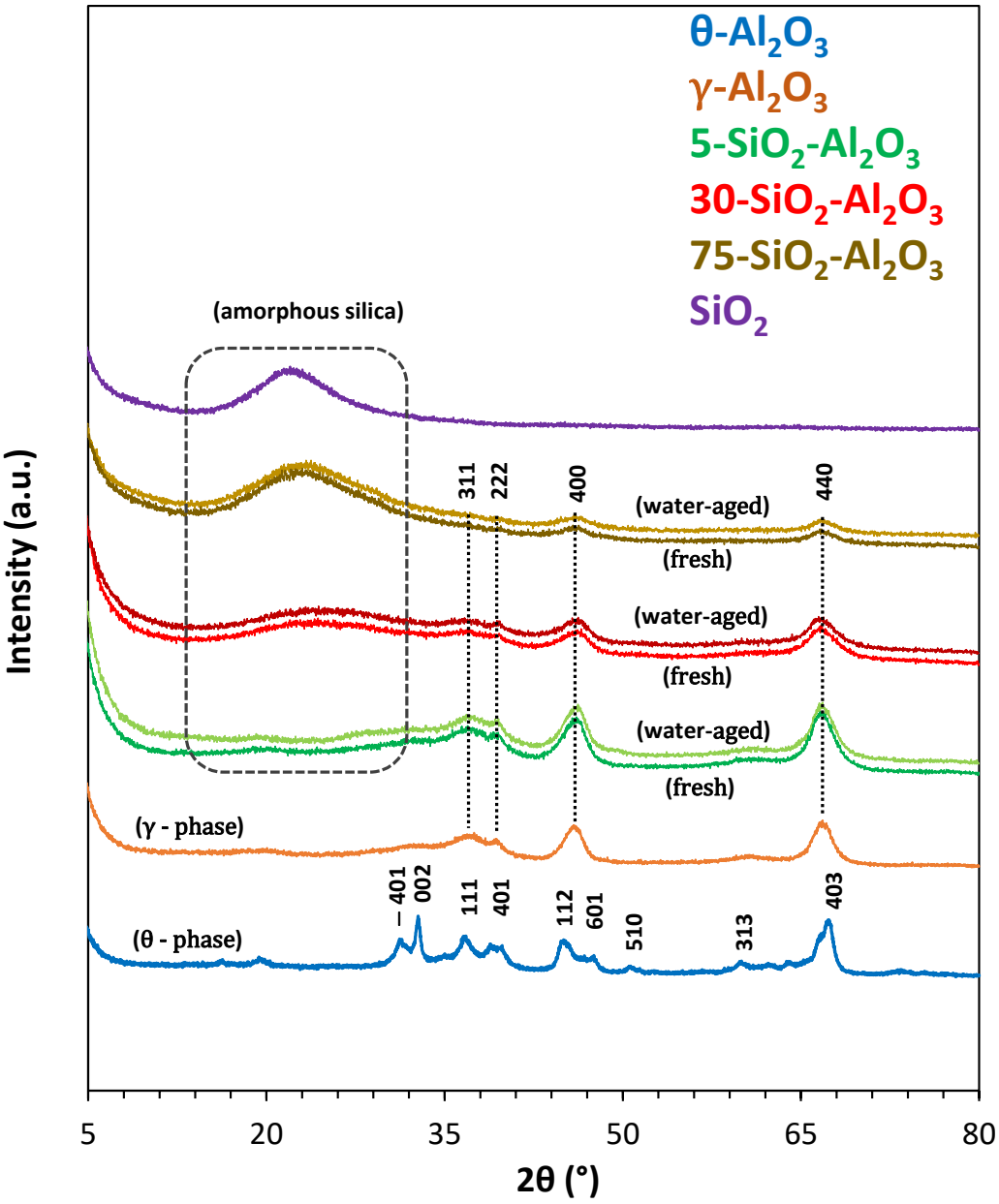

Figure 1. XRD patterns of Al_2O_3 samples, SiO_2-Al_2O_3 solids and SiO_2 powder.

The broad peak at 21.9° for the SiO_2 is attributed to the (111) crystallographic plane. The XRD patterns of different solids suggest that they present a small degree of crystallinity. No changes in diffractograms could be revealed for the water-aged materials. The surface area and porous structure of solids are important parameters in avoiding the diffusion limitations during catalytic testing, by providing abundant surface-active sites that facilitate the catalytic performance and can have an impact for the undesired reactions and the catalyst regeneration. The textural properties of the commercial oxides (as received, denoted as fresh samples and water-aged) were determined from N_2 adsorption–desorption measurements. Table 1 summarises the results obtained, including BET surface area, mean

size of pores, mesoporous (V_{meso}) and total (V_{porous}) pore volumes. Figure 2A,B show the nitrogen adsorption–desorption isotherms and pore-size distributions of different oxides.

Table 1. Textural properties of Al_2O_3, SiO_2-Al_2O_3 and SiO_2 samples.

Catalyst		S_{BET} (m^2/g)	V_{porous} (cm^3/g)	V_{meso} (cm^3/g)	D_p [a] (nm)	Peak of PSD [b] (nm)
θ-Al_2O_3	Fresh	117	0.60	0.57 (≈96%)	20.5	13.1
	Water-aged	121	0.53	0.53	17.5	
γ-Al_2O_3	Fresh	208	0.69	0.68 (≈98%)	13.3	7.5/15.2
	Water-aged	211	0.65	0.65	12.3	
5-SiO_2-Al_2O_3	Fresh	282	0.59	0.58 (≈98%)	8.3	6.5
	Water-aged	317	0.56	0.57	7.1	6.3
30-SiO_2-Al_2O_3	Fresh	373	0.66	0.62 (≈93%)	7.1	5.7
	Water-aged	379	0.68	0.62	7.1	
75-SiO_2-Al_2O_3	Fresh	477	0.36	0.24 (≈65%)	3.0	(<9)
	Water-aged	433	0.31	0.22	2.8	
SiO_2	Fresh	287	1.18	1.13 (96 %)	16.5	13.1

[a] Average BET pore diameter, $D_p \approx \frac{4V_{porous}}{S_{BET}}$; [b] PSD = pore-size distribution in Figure 2B.

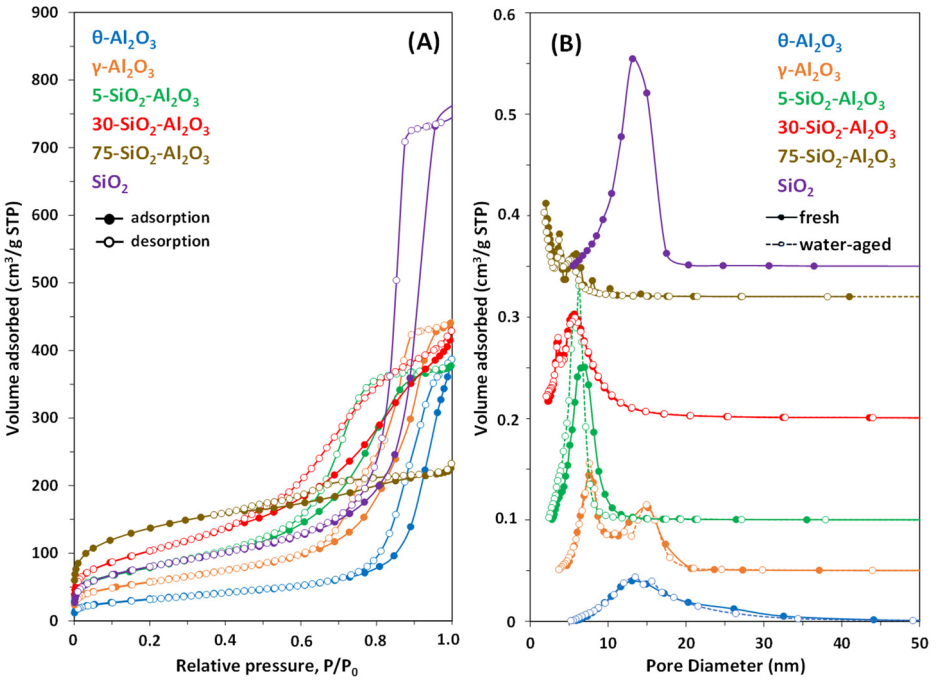

Figure 2. (**A**) N_2 adsorption–desorption isotherms of different solids; (**B**) Pore-size distribution (PSD) of all the samples obtained through the BJH method.

All materials were porous, having BET specific surface areas between 110 and 480 m^2/g. The N_2 adsorption–desorption isotherms of SiO_2, γ-Al_2O_3 and 5-SiO_2-Al_2O_3 samples were of type IV (IUPAC classification), characteristic of mesoporous structures [21]. The increase in N_2 uptake at $P/P_0 < 0.06$ is related to monolayer formation. This is followed by a very slow evolution of the adsorption curve until a P/P_0 of about 0.7, attributed to the transition from monolayer to multilayer adsorption of nitrogen. For $P/P_0 < 0.7$, the adsorption and desorption curves are overlapped for SiO_2 and γ-Al_2O_3, while a hysteresis loop is gradually formed for 5-SiO_2-Al_2O_3 at $P/P_0 > 0.5$. At higher pressures, capillary condensation takes place, which is translated in the adsorption curve by a sharp increase into N_2 uptake until P/P_0 of 0.90−0.95 and an almost constant uptake

at the end of isothermal adsorption. During this last stage, the three samples present a hysteresis loop of H1 type, often associated with porous materials consisting of well-defined cylindrical-like pore channels or agglomerates of approximately uniform spheres [21].

SiO_2 showed the highest saturated adsorption capacity and a monomodal pore-size distribution in the range of 5–20 nm. γ-Al_2O_3 is characterised by two capillary condensation steps at $0.65 < P/P_0 < 0.80$ and $0.80 < P/P_0 < 0.96$ (Figure 2A, the desorption step at high pressures showing a climbing slope). This isotherm shape indicates the bimodal mesoporous character of the material [22,23], as also evidenced by the pore-size distribution plot (Figure 2B). γ-Al_2O_3 is characterised by the presence of mesopores up to 20 nm with maxima around 7.5 and 15.1 nm. 5-SiO_2-Al_2O_3 showed a monomodal pore-size distribution in the range of 2 to 15 nm. The presence of smaller mesopores in the composite oxides, when comparing with SiO_2 and Al_2O_3 samples, is also confirmed for 30-SiO_2-Al_2O_3 and 75-SiO_2-Al_2O_3 powders.

Nitrogen adsorption–desorption isotherms changed from IV types for low content silica sample to a combination of type I and IV for 75-SiO_2-Al_2O_3, indicating a bimodal porous structure for this powder. The 75-SiO_2-Al_2O_3 sample also showed the highest volume of N_2 adsorption at low $P/P_0 < 0.4$, which reflects the presence of micropores along with mesopores in its structure. This is confirmed by data presented in Table 1: except 75-SiO_2-Al_2O_3, all samples present a high percentage (>93%) of mesoporous volume with respect to the total porous volume. 75-SiO_2-Al_2O_3 is characterised by small-sized mesopores (2−5 nm) and an H4-type hysteresis loop characteristic of narrow slip-like pores. 30-SiO_2-Al_2O_3 showed IV-type isotherms with only a slight decrease in the N_2 adsorption rate at the end of isothermal adsorption. The hysteresis loop is close to a H2 type, associated with pores with narrow necks and wide bodies (ink-bottle pores). Diffusion into/from ink-bottle pores is directly related to the width of the neck and may become the rate-determining step for the catalytic process. It is worth mentioning that not only the particular pore shapes but also the connectivity of the pore network plays an important role in determining the extent of hysteresis [21]. 30-SiO_2-Al_2O_3 showed quite narrow pore-size distributions, centred at 5.7 nm.

A similar isotherm type with a smaller volume of N_2 adsorption was also observed for the θ-Al_2O_3 sample, which showed a H3 type hysteresis loop often associated with aggregates of plate-like particles, giving rise to slip-shaped pores. θ-Al_2O_3 was characterised by a broad distribution of pores, stretching into the complete mesopore regime, with a main contribution of 13.1 nm pore size, as shown in Figure 2B.

As summarised in Table 1, the BET surface area of fresh materials increases in the order θ-Al_2O_3 < γ-Al_2O_3 < 5-SiO_2-Al_2O_3 ≈ SiO_2 < 30-SiO_2-Al_2O_3 < 75-SiO_2-Al_2O_3, whereas the total porous volume follows a different trend: 75-SiO_2-Al_2O_3 < θ-Al_2O_3≈ 5-SiO_2-Al_2O_3 < 30-SiO_2-Al_2O_3 < γ-Al_2O_3 < SiO_2. No straightforward relationship between the surface area and pore volume could be deduced from the analysis of the obtained results.

The water-ageing treatment induced only very minor changes (slight increase in surface area) in the textural properties of alumina and 30-SiO_2-Al_2O_3 samples, highlighting their structural stability in the presence of humidity. Note that such a treatment was not performed for pure SiO_2 powder. Water-aged 75-SiO_2-Al_2O_3 showed a reduction in both surface area and pore volume. This may be caused by either the coalescence of microparticles to form larger particles, or by the partial filling/blockage of micropores by water molecules, the removal of which was not complete at an outgassed temperature of 300 °C. The decrease in the average pore diameter observed for all materials could be related to the partial blockage of mesopores. The shape of the sorption isotherm remained unchanged (not shown here for the clarity of Figure 2A). The similar pore-size distribution

of fresh and aged samples could be explained by the variation in the BET surface areas and the pore volumes proportionally to each other.

Interestingly, structural changes of the 5-SiO_2-Al_2O_3 catalyst caused by hot water ageing included the increase in surface area, the disappearance of the residual microporosity and a pore distribution shift towards lower sizes (Table 1 and Figure 2B). A slight increase in BET surface area was already reported in the literature for SiO_2-Al_2O_3 with low loading silica [24] and is explained by structural changes occurring in alumina under hot water. The Al content in 5-SiO_2-Al_2O_3 is high enough to allow its partial reorganisation with the possible formation of gibbsite or boehmite phases, although not detected by XRD.

2.2. Acid–Base Properties of Alumina-Based Catalysts

Adsorption constitutes the primary step of every catalytic reaction involving solid catalysts. Understanding the nature of the adsorbate–adsorbent interaction provides useful insight into the properties of the solid surface. The acidic and basic character of different oxides was studied by adsorption microcalorimetry of NH_3 and SO_2, respectively. The heats evolved are related to the ability of the surface sites to interact with the probe molecules and provide a valuable insight into the strength and distribution of exposed sites.

The differential heats of NH_3 and SO_2 adsorption curves vs. coverage are represented in Figure 3A for pure oxides and in Figure 3B for the silica–alumina catalysts. All samples except SiO_2 show similar features regarding NH_3 adsorption with high initial differential heats (170−200 kJ/mol) related to ammonia adsorption on the strongest sites, followed by a continuous drop in the differential heats with increasing coverage due to adsorption on weaker sites. At high coverage, the values of adsorption heats are characteristic of physisorption or hydrogen-bonded NH_3 (Q_{diff} around 40 kJ/mol). Such behaviour accounts for a heterogeneous distribution of acid site strengths on the solid surface. Both alumina and low-loading SiO_2-Al_2O_3 samples displayed a similar density of acid sites (≈0.8 sites/nm^2), while the acidic character of 30- and 75-SiO_2-Al_2O_3 decreased with increasing silica content.

SiO_2 presents only very weak and very few homogeneous acid sites.

Alumina surfaces exhibit a remarkable chemical heterogeneity with an almost similar amount and strength of acidic and basic sites and can be considered typical amphoteric solids. After the decrease in the differential heat of SO_2 adsorption at very low uptakes, a plateau or a slight decrease in Q_{diff} values is observed (at about 170 kJ/mol), corresponding to heats released during adsorption on the predominant surface sites. At high coverage, the sharp decrease in Q_{diff} accounts for the saturation of the chemisorption sites. The three SiO_2-Al_2O_3 solids preserved the amphoteric character of alumina, but the differential heats of SO_2 adsorption decreased fast and almost monotonically with increasing uptake. Silica–alumina samples are characterised by a lower number of basic sites and lower values of SO_2 adsorption heats on the medium and weak strengths when comparing with pure Al_2O_3.

Table 2 reports, for the fresh oxides, the total NH_3 and SO_2 adsorption uptakes under an equilibrium pressure of 27 Pa and the chemisorbed ones calculated at the same pressure from the difference between the adsorption and readsorption isotherms (see experimental section). The ratio $Q_{int,total}/n_{total}$ was also calculated and reported in Table 2. $Q_{int,total}$ is the integral heat representing the total heat of adsorption evolved under an equilibrium pressure of 27 Pa and so is associated with the solid acid or basic site density. $Q_{int,total}/n_{total}$ values may be taken as a criterion to compare the average strength of the main exposed acid and basic sites, knowing that the heats of adsorption correspond to an average over all adsorbed surface species. Both Al_2O_3 samples presented similar basicity, in number and strength, when considering their surface areas.

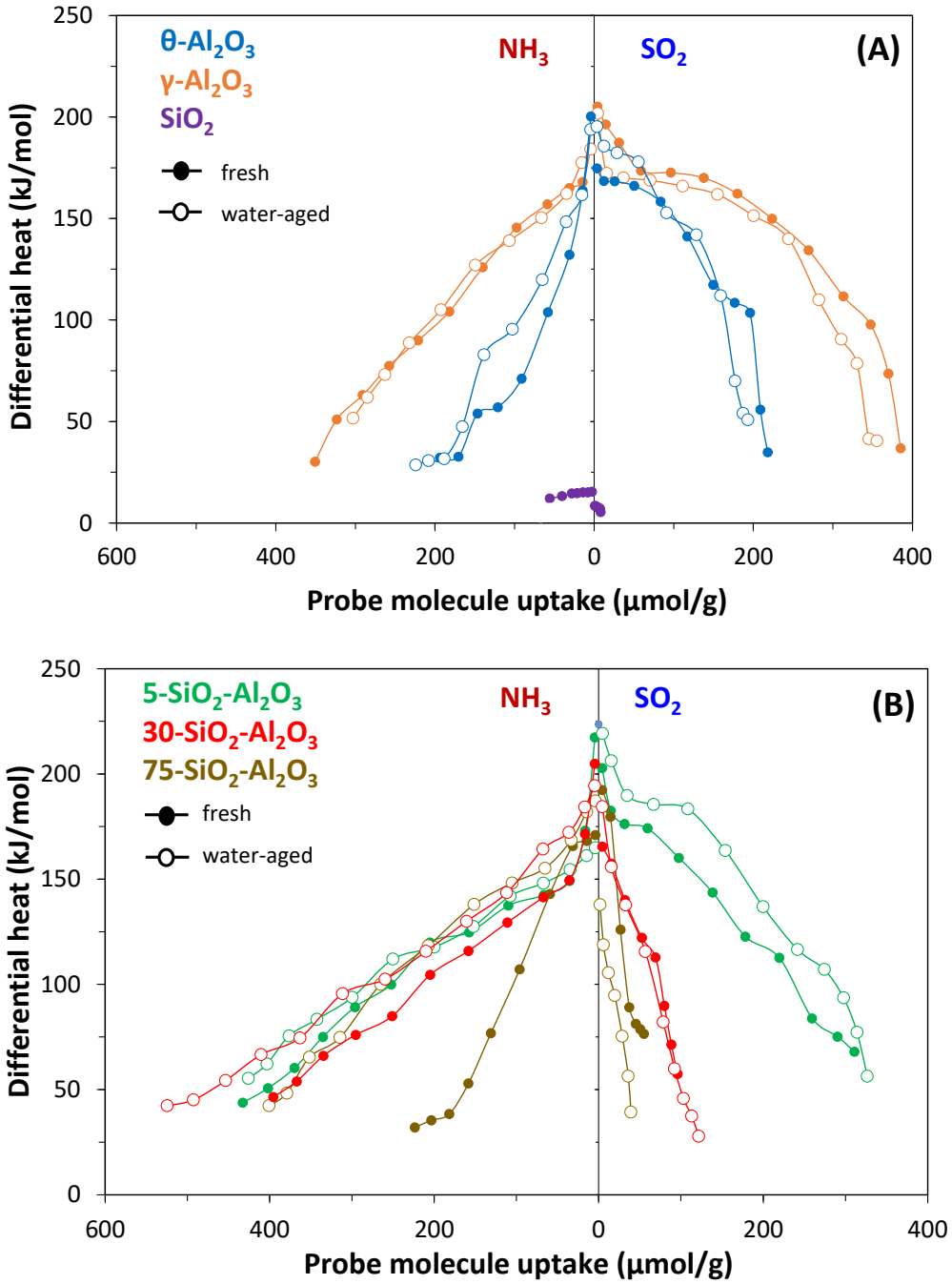

Figure 3. Differential heats of NH_3 and SO_2 adsorption at 150 °C versus the respective coverage by the probe on (**A**) Al_2O_3 and SiO_2 pure fresh and water-aged oxides and (**B**) SiO_2-Al_2O_3 catalysts (fresh and water-aged). Prior to microcalorimetric experiments, all powders were outgassed at 400 °C overnight.

The surface density of acid sites is slightly higher for γ-Al_2O_3, which also showed the strongest interaction with NH_3 between studied oxides. SiO_2-Al_2O_3 samples were characterised by lower surface densities of active sites (sites/nm^2) with respect to aluminas, and this gap increases with increasing amounts of SiO_2.

The number of strong acid sites ($n_{irrev}(NH_3)$) increased with the Si/Al ratio up to 30, when compared with pure γ-Al_2O_3, from 164 to 225 µmol/g (Table 2). Then, the number of strong acid sites strongly decreased for high silica-loading in 75-SiO_2-Al_2O_3 with 109 µmol/g.

Acid–Base properties were studied in fresh samples but also after water-ageing, except with SiO_2. The evolution of differential heats of NH_3 and SO_2 adsorption at 150 °C with coverage is displayed in Figure 3A,B. Table 3 gives the strength distribution of the acid sites.

Table 2. Calorimetric data for NH_3 and SO_2 adsorption at 150 °C for as-received oxides.

Sample	$Q^{NH_3}_{int,total}/n_{total}$ (kJ/mol) [a]	NH_3 Uptake (μmol/g)		$Q^{SO_2}_{int,total}/n_{total}$ (kJ/mol) [a]	SO_2 Uptake (μmol/g)	
		n_{total} [b*]	n_{irrev} [c*]		n_{total} [b*]	n_{irrev} [c*]
θ-Al_2O_3	95	157 (0.81)	60 (0.31)	145	200 (1.03)	152 (0.78)
γ-Al_2O_3	123	293 (0.85)	164 (0.47)	154	351 (1.02)	286 (0.83)
5-SiO_2-Al_2O_3	121	364 (0.78)	194 (0.41)	139	280 (0.60)	211 (0.45)
30-SiO_2-Al_2O_3	116	337 (0.54)	225 (0.36)	135	81 (0.13)	50 (0.08)
75-SiO_2-Al_2O_3	112	187 (0.24)	109 (0.14)	144	49 (0.06)	28 (0.04)
SiO_2	13	30 (0.06)	9 (0.02)	16	6 (0.01)	5 (0.01)

[a] $Q_{int,total}$ is the integral heat of adsorption corresponding to n_{total}. [b] Amount of probe adsorbed under an equilibrium pressure of 27 Pa. [c] Amount of NH_3 and SO_2 irreversibly chemisorbed. [*] In the brackets, the average surface densities of sites are given (sites/nm^2)

Table 3. Population of acid sites (μmol NH_3/g solid) with a given strength (kJ/mol) for fresh and water-aged solids.

Sample		<100	100−150	>150
θ-Al_2O_3	fresh	95	40	22
	water-aged	85	63	33
γ-Al_2O_3	fresh	99	111	82
	water-aged	61	137	68
5-SiO_2-Al_2O_3	fresh	112	217	35
	water-aged	81	225	57
30-SiO_2-Al_2O_3	fresh	121	188	35
	water-aged	153	180	98
75-SiO_2-Al_2O_3	fresh	83	54	51
	water-aged	74	171	95

The water-ageing process produced additional acid sites responsible for the enhanced acid character of SiO_2-Al_2O_3 catalysts, and this becomes more pronounced with the increase in the silica content. For water-aged 75-SiO_2-Al_2O_3, the density of acidic sites is more than doubled in comparison with the fresh sample (0.5 versus only 0.2 sites/nm^2 for the fresh sample under an equilibrium pressure of 27 Pa).

New medium and strong acid sites appeared. The increase in the acidic character observed could be caused by the development of partly uncovered alumina on the surface during the hydrothermal treatment. However, no increase in the basic character was observed (Figure 3B, left side). The increase in acidity could be caused by the formation of new Brönsted sites (e.g., Si(OH)Al, Si-Al(OH)-Si, Q ≈ 100−150 kJ/mol) and of some coordinatively unsaturated aluminium atoms (Q > 150 kJ/mol) in a geometric environment similar to that of Lewis acidic sites on alumina. To a lesser extent, the same behaviour was observed for 30-SiO_2-Al_2O_3, with average density of acid sites increasing from 0.5 sites/nm^2 for the fresh powder to 0.7 for the water-aged one while preserving the basic character. The weak strengths (Q < 100 kJ/mol) of acid sites could be related to the development of Brönsted acid sites such as SiOH or AlOH type during ageing together. 5-SiO_2-Al_2O_3 preserved the amount of acid sites, but a detailed examination of the differential heat curve shows a redistribution of their strengths with the decrease in the number of the weakest sites (Q < 100 kJ/mol) and the increase in the number of medium- (150 > Q > 100 kJ/mol)

and high- (Q > 150 kJ/mol) strength sites (Table 3). It was observed that the strongest basic sites also emerged after hot-water treatment.

Regarding pure aluminas, the results obtained show the overall stability of their acid–base character, although the distribution of the active sites (surface hydroxyls and aluminium cations embedded in a specific neighbourhood [25]) seems slightly different when comparing water-aged and fresh samples.

The catalytic properties of oxides are intimately linked to their surface properties. The steam added or formed during reaction can induce changes in the acid–base site distribution of silica–alumina solids.

2.3. ^{29}Si and ^{27}Al NMR

The coordination of aluminium and silicon in fresh powders was examined by ^{27}Al and ^{29}Si NMR spectroscopy. The spectra obtained are given in Figure 4A,B. The ^{27}Al chemical shifts depend primarily on the coordination of aluminium with respect to oxygen. Generally, chemical shifts from 55 to 80 ppm are assigned to tetrahedral coordination of aluminium, while octahedral Al shows a resonance signal at 0−22 ppm [26].

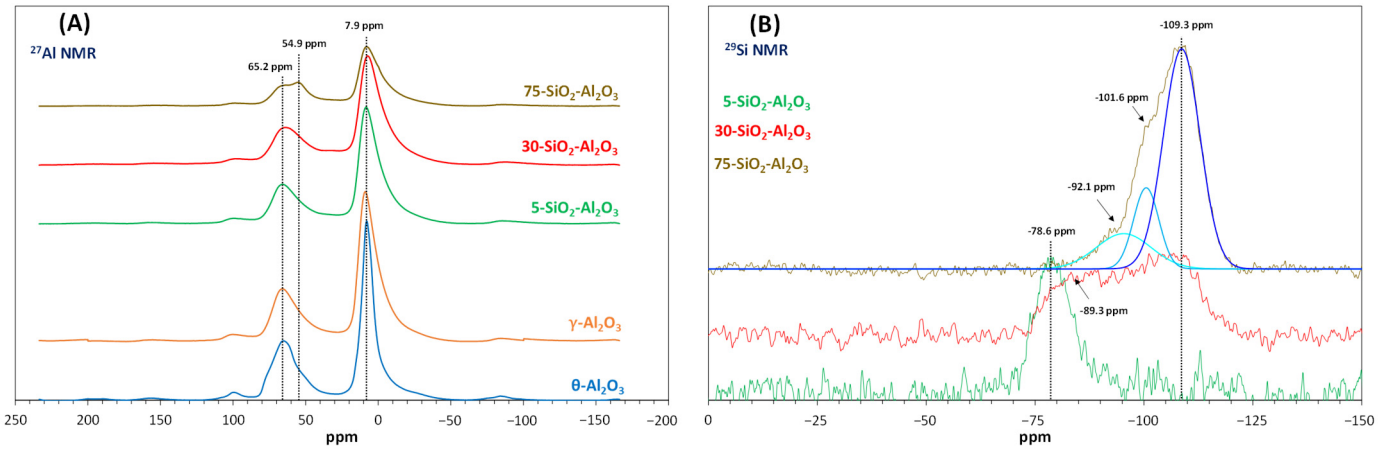

Figure 4. (**A**) ^{27}Al MAS NMR spectra of fresh Al_2O_3 and SiO_2-Al_2O_3 samples and (**B**) ^{29}Si spectra for as-received silica–alumina powders.

On the other hand, the ^{29}Si chemical shifts when Si-O ligands are exchanged for Al-O ligands can be used to determine the structure and the degree of homogeneity of SiO_2 distribution in silica–alumina powders [27].

NMR spectra of ^{27}Al (Figure 4A) are characterised by an intense resonance signal at 8 ± 0.8 ppm, a large peak at 65.5 ± 0.5 ppm and several spinning side bands. The chemical shifts at 8 and 65 ppm reveal the presence of six- and four-coordinated Al, respectively. The Al^{VI}/Al^{IV} ratio varied in the following order: 5-SiO_2-Al_2O_3 (2.2) > 30-SiO_2-Al_2O_3 and γ-Al_2O_3 (2.1) > 75-SiO_2-Al_2O_3 (1.9) > θ-Al_2O_3 (1.7). The coordination number of the surface aluminium atoms in SiO_2-Al_2O_3 samples is consistent with the corresponding value of a spinel type of alumina such as γ-Al_2O_3, [28]. The ^{27}Al signal for 75-SiO_2-Al_2O_3 shows two contributions, at 54.9 and 65.2 ppm, indicating the presence of crystallographically non-equivalent sites for tetrahedral Al (e.g., Al in alumina and aluminium isomorphously substituting Si^{4+} in silica).

Figure 4B displays the changes in ^{29}Si chemical shifts with increasing silica content in the mixed oxides. 5-SiO_2-Al_2O_3 showed only one well-defined peak at ca. −78 ppm, a lower frequency shift than expected. Indeed, in NMR studies for amorphous aluminosilicates, ^{29}Si chemical shifts are observed in the region from ca. −83 to −115 ppm [26,29]. For example, the chemical shift assignments suggested by Man at al. [30] are as follows: Q^4[Si(2Al)],

$Q^3[(SiO)_2(AlO)SiOH]$ and $Q^2[(SiO)_2Si(OH)_2]$ at −92 ppm; Q^4[Si(1Al)] and $Q^3[(SiO)_3SiOH]$ at −101 to −102 ppm; Q^4[Si(0Al)] at −108 to −111 ppm. In Q^n, *n* refers to the number of bridging oxygens around a central silicon atom, while *m* in [Si(*m*Al)] is the number of Al atoms substituting Si atoms in the first layer. Based on the work of McMillan et al. [27], the resonance band at −78 ppm seems to represent silica units bonded to the surface of alumina in a strained environment. The authors [27] observed a good correlation between the stabilisation of the alumina porosity and the amount of the −78 ppm surface framework species formed by silica addition. This result showed that 5-SiO_2-Al_2O_3 is most probably a mechanical mixture of two oxides rather than a solid solution.

For 30-SiO_2-Al_2O_3, a broad resonance band between −80 and −125 ppm was measured, which may be dominated by resonance chemical shifts at −89 and −107 ppm. Such spectra could contain all characteristic signals of silicates from Si(0Al) to Si(4Al). Due to the low signal-to-noise ratio, the distribution of different Si species was not determined.

With increasing the Si content, this band becomes narrower with a maximum at −109 ppm and two visible shoulders at ca. −102 and −92 ppm. Careful fits indicate the presence of 67% of bulk silica (silicon coordinated to four silicate tetrahedra expressed as Si(0Al) at −109 ppm), which may explain the acid character decrease observed by adsorption microcalorimetry. In addition, the resonance peaks at −102 and −92 ppm, in similar proportion (17 and 16%, respectively), are most probably related to [Si(1Al)] and [Si(2Al)] species, respectively. These chemical shifts may also correspond to the terminal $(SiO)_3SiOH$ and the geminal $(SiO)_2Si(OH)_2$ tetrahedra as well as to $(SiO)_2(AlO)SiOH$ groups [31].

The ^{1}H MAS-NMR spectra for silica–alumina are displayed in Figure 5. The shapes of all spectra are qualitatively the same whatever the Si/Al ratio, with one Lorentzian type resonance peak at a chemical shift of ca 4.5 ppm, the intensity of which increases with SiO_2 amount. Dorémieux-Morin et al. [32] attributed this signal to protons in fast chemical exchange between mainly acidic OH groups and water molecules. The additional Gaussian signals observed for 30-SiO_2-Al_2O_3 could be assigned to silanol groups or to acidic bridging OH groups [31].

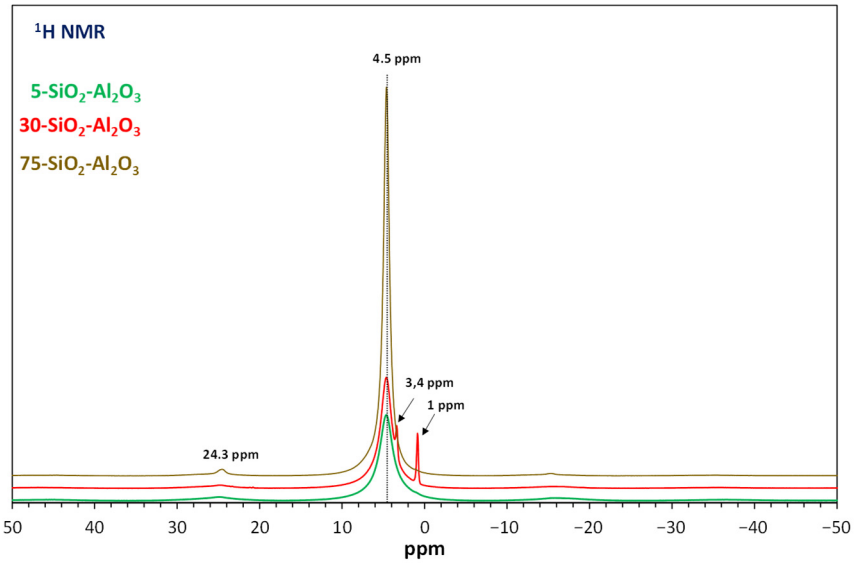

Figure 5. ^{1}H NMR spectra of fresh Al_2O_3 and SiO_2-Al_2O_3 samples.

2.4. FTIR Study

The structural characterisation of silica–alumina powders was further performed by Fourier-transformed infrared spectroscopy. Figure 6 shows the infrared spectra for fresh

samples, including pure alumina and silica, and water-aged SiO_2-Al_2O_3. The spectra of alumina powders are similar to those reported in the literature for γ and θ phases [33,34], being consistent with XRD analysis. γ-Al_2O_3 is characterised by vibrations in the region of 1200−400 cm^{-1} with two broad contributions at about 627 and 804 cm^{-1}. The former one corresponds to the Al-O-Al stretching mode of condensed AlO_6 octahedra, generally occurring in the range of 400−750 cm^{-1} [34]. The second contribution is related with the stretching mode of a lattice of condensed or interlinked AlO_4 tetrahedra reported in the region of 750−900 cm^{-1} [33]. The large bands account for the disorder in the cation distribution in this phase. The additional broad absorption observed as a shoulder in the region 1100−950 cm^{-1} is indicative of surface species involving tetrahedral Al cations [35]. For θ-Al_2O_3, the same contributions could be observed at about 573 and 828 cm^{-1}, partly resolved into several sharp components associated with the ordering of cation vacancies into clusters in octahedral sites (higher crystalline order is achieved in the theta phase when comparing with the defective spinel-type of gamma-phase) [33,36]. Both samples are also characterised by (i) a broad band in between 3200 and 3700 cm^{-1} assigned to -OH stretching vibration that is bonded to Al^{3+} and (ii) a band at ≈ 1630 cm^{-1} corresponding to physisorbed water. It is worth mentioning that these two contributions are present in all analysed oxides (Figure 6). Additionally, SiO_2 showed an intense band at ca. 1100 cm^{-1} attributed to asymmetric stretching vibrations of Si-O-Si [37]. The symmetric stretching vibrations of Si-O-Si and its bending mode were observed at ca. 804 and 471 cm^{-1}, respectively.

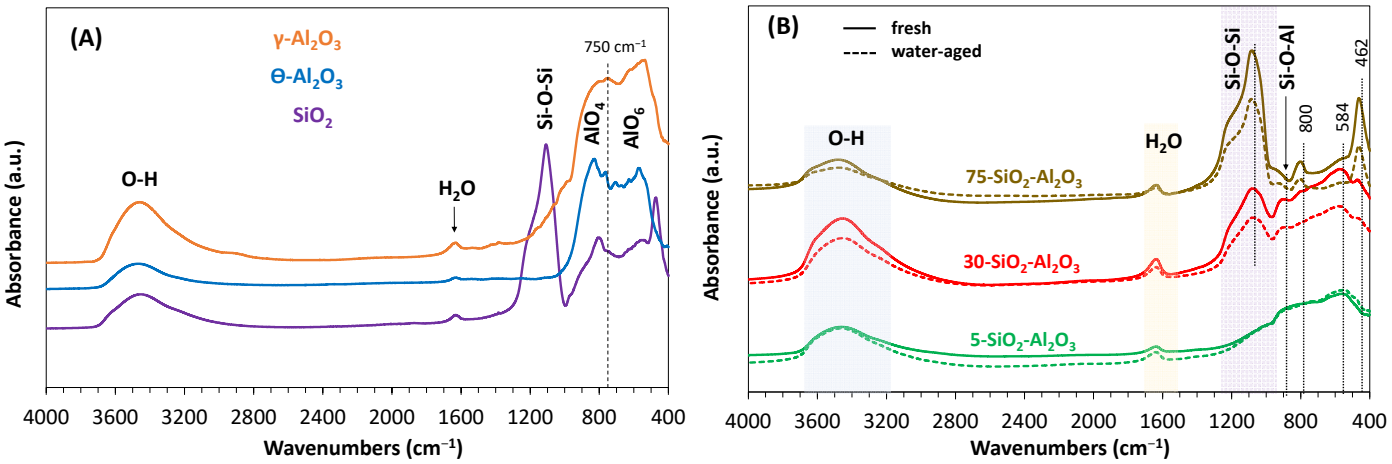

Figure 6. FT-IR spectra of KBr-pellets of fresh catalysts and water-aged SiO_2-Al_2O_3 samples. (**A**) Pure, as-received, Al_2O_3 and SiO_2; (**B**) SiO_2-Al_2O_3 fresh and water-aged powders.

The SiO_2-Al_2O_3 samples showed an IR fingerprint of both silica and alumina components:

(i) The FTIR spectrum of 5-SiO_2-Al_2O_3 shows a similar shape to that observed for γ-Al_2O_3, with more broad and less defined vibrations, most probably due to the overlapping of bands related to Al-O and Si-O, all appearing in the 1200−400 cm^{-1} region. The Al-O-Al stretching mode of condensed AlO_6 octahedra is clearly observed at ca. 584 cm^{-1}, while the band between 750 and 1000 cm^{-1} may contain both contributions deriving from lattice AlO_4 tetrahedra and stretching vibrations of the Si-O-Al bond. No well-defined absorption related to Si-O-Si stretching bands could be observed.

(ii) With increasing silica content in SiO_2-Al_2O_3, the Si-O stretching vibration mode of Si-O-Si groups appeared at ca. 1077, 800 and 460 cm^{-1} accompanied by the band characteristic of octahedral coordination of Al^{3+} ions. The new vibration between 1000 and 800 cm^{-1} may be related to the interaction of Si and Al atoms with the formation of a SiO_2-Al_2O_3 amorphous phase.

(iii) Though FT-IR spectroscopy could give information about the changes provoked by ageing, the similar features observed for fresh and water-aged powders in Figure 6B show that the SiO_2-Al_2O_3 structure was minimally affected by the soft hydrothermal process applied.

The nature of the acid character of silica–aluminas was recently reviewed by Busca [38,39] based on IR experiments, structural considerations and theoretical studies. Brönsted acid sites were associated with the terminal silanols not bridged but activated by nearby Al^{3+} ions. The improved acid character of silica rich water-aged materials could be the result of such medium-strength Brönsted sites formed, together with small numbers of strong Lewis sites, during the hydrothermal treatment by the migration of some aluminium ions in the amorphous silica phase. In 5-SiO_2-Al_2O_3, acid–base couple sites were created by treatment in hot water.

NH_3 adsorption–desorption FT-IR was further used to assess the nature of the acid sites and their strengths. Before adsorption, all samples were thermally treated under oxygen flow up to 400 °C and outgassed under a vacuum at 400 °C. The FT-IR spectra in the OH stretching region after this pre-treatment are displayed in Figure 7A. 75-SiO_2-Al_2O_3 showed a noisy spectrum and is not displayed in the figure for the clarity reasons. Similarly to what was already reported [35], the pure Al_2O_3 spectrum shows three well-defined bands at ≈3770, 3726 and 3679 cm^{-1}, which were assigned, respectively, to (1) terminal OH groups over one tetrahedrally coordinated Al ion, either in a non-vacant environment or near a cation vacancy; (2) terminal OH over an octahedrally coordinated Al ion; and (3) bridging OH groups. Spectra of 5-SiO_2-Al_2O_3 appear similar to those of γ-Al_2O_3, with a band at 3726 cm^{-1} showing a tail to higher wavenumbers, in the region of O-H stretching of surface silanol groups. Indeed, over pure silica, this vibration is found at 3745 cm^{-1}. The increased silica content in the mixed oxides is accompanied by a growth in the surface silanol band, while the absorption related to surface hydroxyl groups bonded to tetrahedral aluminium ions appears only as a shoulder at 3743 cm^{-1}. The surface phase contains fewer concentrated tetrahedral Al ions with increasing amounts of SiO_2, in accordance with NMR date and calorimetric results.

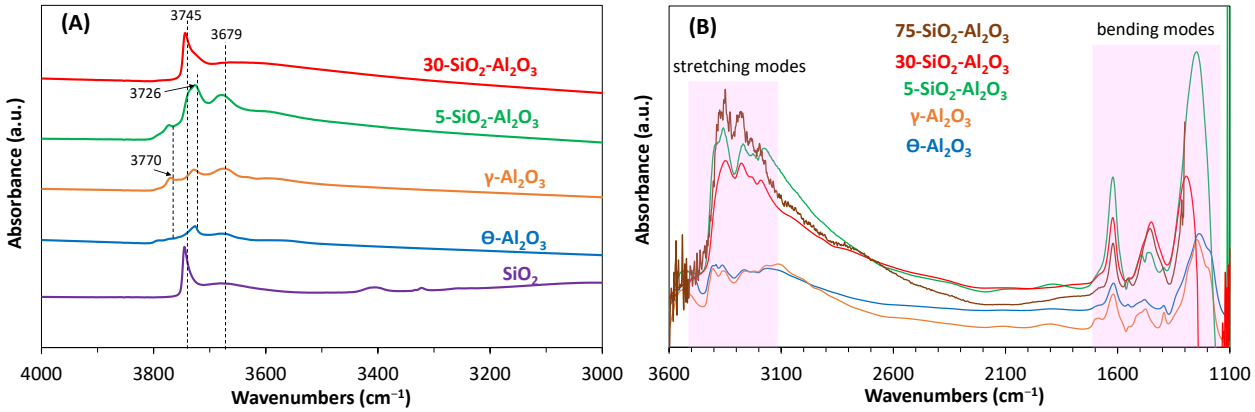

Figure 7. (**A**) Comparison of FT-IR spectra (OH stretching region) of the different solids after outgassing at 400 °C. (**B**) FT-IR spectra of catalysts with adsorbed NH_3 at 25 °C after evacuation for 30 min at 25 °C.

The IR bands characteristic of the N-H stretching and bending asymmetric/symmetric vibrations in gaseous ammonia are observed, respectively, at 3444/3336 cm^{-1} and 1628/950 cm^{-1} [40]. Figure 7B displays the NH_3−FTIR spectra obtained after exposing the outgassed solids to 15 mbars of NH_3 vapour for 1 h, evacuating for 30 min, both at 25 °C, and subtraction of the spectra registered after outgassing treatment at 400 °C. In the O-H stretching frequency region, the adsorption of ammonia gave rise to a large

band at ≈3350 cm^{-1}, partly resolved into several components, with a tail towards lower wavenumbers. The bands at ≈1620 cm^{-1} and 1100–1350 cm^{-1} in the bending vibration region of ammonia are assigned to NH_3 coordinated species to Lewis acid sites. In the region of low wavenumbers, the band at ≈1440 cm^{-1} is characteristic of NH_4^+ ions formed at Brönsted acid sites (proton-donating sites of the surface). The intensity of this last band increased with increasing silica content in the mixed oxides.

Since the N-H stretching region is not well-resolved, the differences in spectra of various forms of adsorbed ammonia with the temperature will be further followed in the N-H bending region.

Figure 8 shows the evolution of NH_3 adsorbed species when evacuating the samples at 25, 100, 200 and 300 °C. When NH_3 is admitted to pure alumina samples, bands at ≈ 1242, 1390, 1474, 1618 and 1696 cm^{-1} of adsorbed ammonia appeared in the spectrum. As the pumping temperature increases, the intensity of all bands progressively decreases. At 300 °C, all signals vanish, except the band at 1242 cm^{-1}, which becomes narrower and shifts at higher wavenumbers (1275 cm^{-1} at 300 °C). This shift was expected to be related to the strength of the bond formed (the higher the wavenumber, the higher the stability of the bond). Further, the broad band at 1242 cm^{-1} with shoulders at ≈1200 and 1280 cm^{-1} (broad with shoulders), assigned to coordinated ammonia molecules (symmetric deformation) [40,41], is characteristic of heterogeneous Lewis acid sites, in good agreement with adsorption microcalorimetric data. The corresponding asymmetric deformation band of coordinated ammonia species appeared at 1618 cm^{-1}. Bands found at 1696 cm^{-1} (symmetric deformation) and 1474 cm^{-1} (asymmetric deformation) are characteristic of NH_4^+ ions. The presence of the shoulder at 1516 cm^{-1} and the band at 1390 cm^{-1}, and the assumed the presence of Brönsted acid sites, account for ammonia adsorbed on different OH species. Finally, the small band at ≈1550 cm^{-1} accounts for a small amount of -NH_2 surface groups.

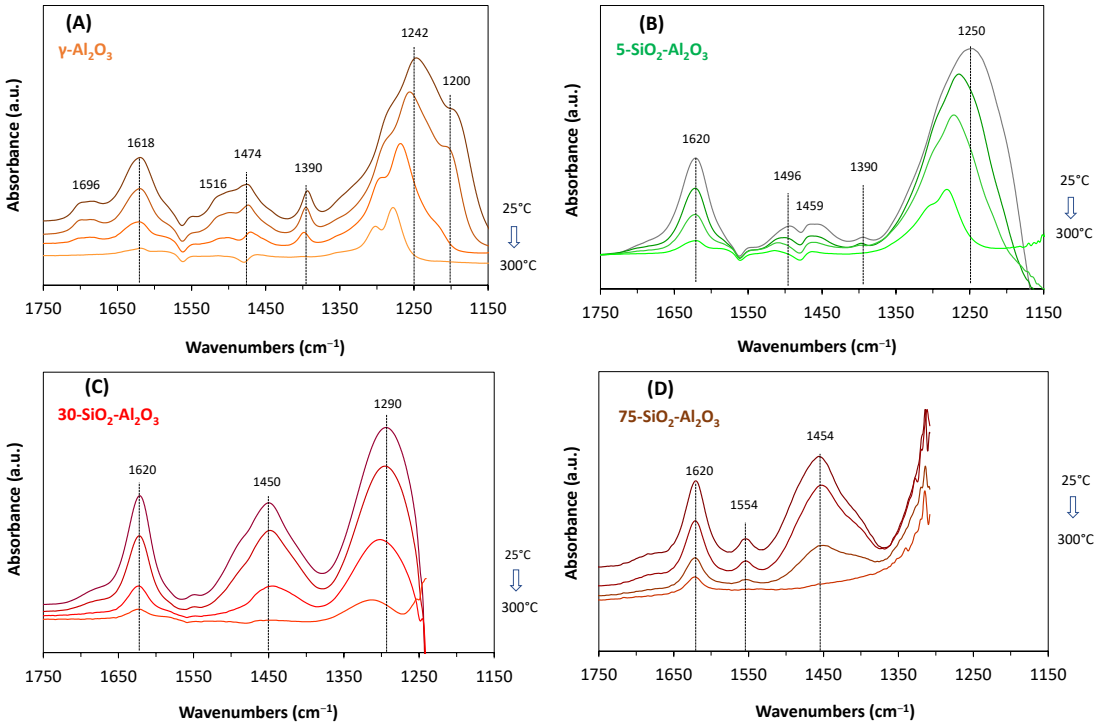

Figure 8. FT-IR spectra of γ-Al_2O_3 (**A**) and 5 SiO_2-Al_2O_3 (**B**), 30 SiO_2-Al_2O_3 (**C**) 75 SiO_2-Al_2O_3 (**D**) solids with adsorbed ammonia and after outgassing at 26, 100, 200 and 300 °C. θ-Al_2O_3 presented a similar behaviour to γ-Al_2O_3 and is not shown here. Ammonia adsorbed on surface hydroxyl groups of SiO_2 was completely removed by pumping at 25 °C.

The results obtained evidenced that, at the reaction temperature of the targeted application here, the acidity of alumina is mostly of Lewis type with high-strength sites (Q > 150 kJ/mol, Table 3) as determined by NH_3 adsorption microcalorimetry. However, it is worth mentioning that during catalytic testing (between 200 and 300 °C), water vapours are produced by IPA dehydration, and the strong Lewis acid sites will be partly hydrated. Indeed, the electron-pair vacancy of aluminium is filled by the sharing of one of the free electron-pairs of the oxygen in water, making one of the protons of water readily ionizable, which will react as Brönsted acid sites [42]. Further, a decrease in the strength of Lewis acid sites on γ-Al_2O_3 is expected under reaction conditions in the presence of water, as found by Li and Shen [43].

The low-silica-content SiO_2-Al_2O_3 (Figure 8B) showed similar properties to γ-alumina. Characteristic bands for both NH_3 (1620 cm^{-1}) and NH_4^+ (1496, 1459, 1390 cm^{-1}) appeared in the spectrum of 5-SiO_2-Al_2O_3 together with a small signal at ≈ 1550 cm^{-1}. The latter band, assigned to –NH_2 species formation by NH_3 dissociation on a suitable acid–base site, became better-defined with increasing silica content. In all samples, the Lewis acid sites are predominant at 300 °C, while at 200 °C, both Lewis- and Brönsted-type acid sites are present on the surface of SiO_2-Al_2O_3 powders. Larmier et al. [13] showed that the Brönsted moiety in silica–alumina helps to stabilise the transition state such as the -OH leaving group in isopropanol dehydration when comparing with the naked Al Lewis site. The authors [13] found that the most likely active acid sites in isopropanol dehydration on amorphous silica–alumina are the so-called "pseudo bridging silanols", dual sites with both Lewis and Brönsted functions. The synergy between SiOH and Al sites in silica–alumina, leading to the formation of pseudo-bridging silanol groups, was also evidenced by Chizallet and Raybaud [44].

The fraction of sites that bond NH_3 between 200 and 300 °C is expected to play a role in the catalytic performances of studied solids in isopropanol dehydration to propylene.

2.5. Catalytic Conversion of IPA

The catalytic activity of the commercial oxides was initially tested as a function of the reaction temperature in the range of 200–300 °C. Table 4 shows the IPA conversion and selectivities of the formed products at different temperatures. At 200 °C, the conversion varied between 1.0 % for θ-Al_2O_3 and 100 % 75-SiO_2-Al_2O_3, with PEN being the only product detected. 75-SiO_2-Al_2O_3 showed complete conversion of isopropanol between 200 and 300 °C, while SiO_2 presented low activity in all temperature ranges. For the other alumina-based catalysts, as the temperature increased to 250 °C, the conversion of IPA increased to 100 %, except with θ-Al_2O_3. At 300 °C, the isopropanol was completely converted over all Al_2O_3 catalysts. The high selectivity for propylene formation was preserved at all studied temperatures, with only traces of ACE being detected, mostly at 300 °C. For SiO_2, the increase in the reaction temperature induced the enhancement of the conversion and dehydrogenation pathway, with acetone selectivity up to 21.5%. However, the conversion and yields of PEN and ACE are negligible for pure silica in comparison with Al_2O_3 and SiO_2-Al_2O_3.

At low temperatures, gamma-alumina exhibits 10-fold superior activity to θ-Al_2O_3. Interestingly, both alumina samples present similar average surface densities of 1.01 ± 0.01 basic sites per nm^2 and 0.83 ± 0.02 acid sites per nm^2 when taking into account the total adsorbed SO_2 and NH_3, respectively, under an equilibrium pressure of 27 Pa at 150 °C. Differences found when taking into account the density of the strong chemisorption acid sites (0.47 sites/nm^2 for γ-Al_2O_3 over 0.31 sites/nm^2 for θ-Al_2O_3) and the average strength of the main exposed acid sites (Table 2, second column), in agreement with the literature findings [45], can justify the difference of reactivity between the aluminas.

The activity gap between alumina samples decreases with increasing temperature, and at 300 °C, IPA is completely converted on both catalysts in the experimental conditions used here. No further comparison can be made concerning the number and the strength of active sites, since only a fraction of these sites are necessary to achieve full conversion.

Table 4. Isopropanol conversion over Al_2O_3 and silica–alumina catalysts. Reaction conditions: catalyst volume, 0.1 mL; He flow rate, 28.5 mL/min; feed rate of IPA, 1.5 mL/min (1.5/30 = 5%). Pure IPA at 23 °C was used as the reactant.

Catalyst [a]	Temperature (°C)	Conversion [b] (%)	Selectivity [b] (%)		PEN Formation Rate [c]	
			PEN	ACE	(mol/g·s)	(*mol/mL·s*)
θ-Al_2O_3 (49.4 mg)	200	1.0	100	0.0	2.1×10^{-7}	0.104×10^{-7}
	250	18.8	100	0.0		
	275	61.8	100	0.0		
	300	100	99.7	0.3		
γ-Al_2O_3 (57.7 mg)	200	42.6	100	0.0	7.6×10^{-6}	4.385×10^{-7}
	250	100	99.9	0.1		
	300	100	99.6	0.4		
5-SiO_2-Al_2O_3 (65.7 mg)	200	33.7	100	0.0	5.3×10^{-6}	3.382×10^{-7}
	250	100	99.9	0.1		
	300	100	99.6	0.4		
30-SiO_2-Al_2O_3 (47.6 mg)	200	81.2	100	0.0	1.8×10^{-5}	8.568×10^{-7}
	250	100	100	0.0		
	300	100	99.7	0.3		
75-SiO_2-Al_2O_3 (65.7 mg)	200	100	100	0.0	$>1.6 \times 10^{-5}$	$>10.512 \times 10^{-7}$
	250	100	100	0.0		
	300	100	99.7	0.3		
SiO_2 (35.0 mg)	200	4.9	100	0.0	1.4×10^{-6}	0.49×10^{-7}
	250	5.6	81.9	18.1		
	300	8.2	78.5	21.5		

[a] The amount of catalyst used in the catalytic test. [b] Average value in 2 h. (PEN = propylene; ACE = acetone). [c] PEN formation rate = $\frac{\text{IPA conversion}}{100} \times \frac{\text{IPA flow}}{V_m} \times \frac{273}{296} \times \frac{1}{m_{catalyseur}}$, with IPA flow of 1.5 mL/min.

Depending on the silica-to-alumina ratio, SiO_2-Al_2O_3 samples presented different characteristics in terms of acid/base (strength and density) and textural properties. As seen in Table 4, the dehydration efficiency in terms of IPA conversion, at 200 °C, increases with the silica loading. The improvement of the catalytic performance with silica content may be explained by the combined action of the increase in specific surface area of the catalyst, different porous structure and acid/base properties induced by the increase in the Si/Al molar ratio. At 250 and 300 °C, the IPA was completely consumed over all three catalysts.

No direct correlation between the number of the total or strong acid sites determined by adsorption microcalorimetry for the fresh samples and the catalytic activity at 200 °C could be established. On the contrary, when comparing the activity results at 200 °C with the adsorption calorimetry data of water-aged powders, it was found that the IPA conversion correlates well with the proportion of high-strength sites (Q > 150 kJ/mol, Table 3), as seen in Figure 9.

75-SiO_2-Al_2O_3 catalyst was not considered for this comparison, already giving 100% conversion at 200 °C, while SiO_2 was not studied under water-aged conditions.

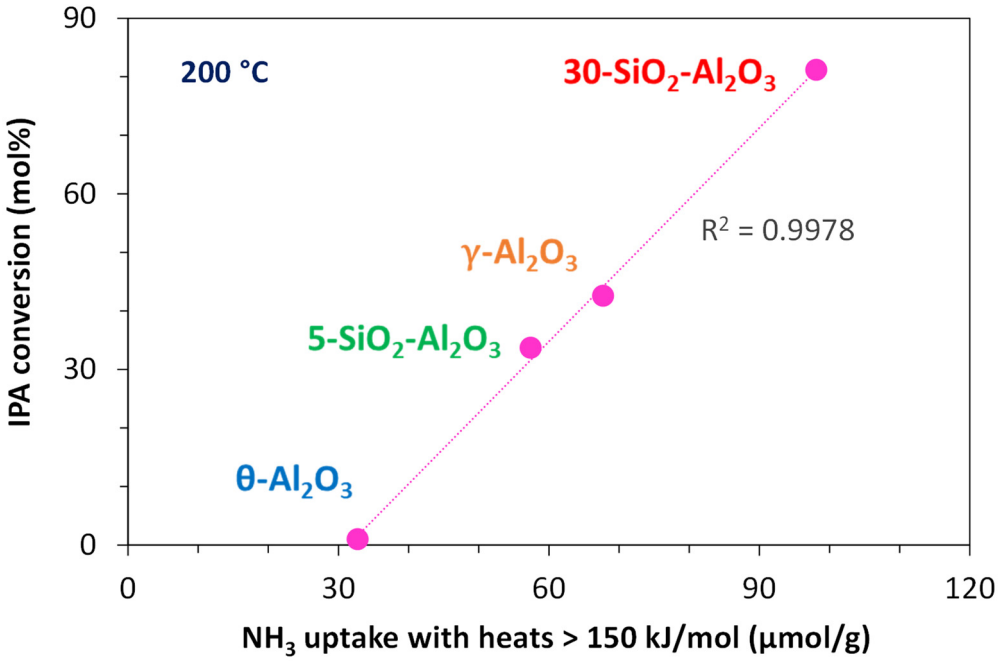

Figure 9. Evolution of the IPA conversion at 200 °C with the amount of strong acid sites determined by NH_3 adsorption microcalorimetry at 150 °C for water-aged catalysts. 75-SiO_2-Al_2O_3 showed 100 % conversion at 200 °C.

Although the highest conversions were measured for 75-SiO_2/Al_2O_3, it should be noted that this catalyst suffered the most significant changes in the textural and acid properties during hydrothermal treatment. Compared with 30-SiO_2-Al_2O_3, fresh and water-aged 75-SiO_2/Al_2O_3 samples are characterised by a lower density of acid/base sites but present a higher BET surface area and a narrower distribution of pore size with both micro-and meso-pores.

Although the catalytic activity of solid acids may also be related to their textural properties, no linear-dependence relationship between the converted IPA at 200 °C and the BET surface area, the mean pore diameter or porous volume taken independently could be established. From Mitsui's patent [46], the key features of alumina performing in IPA dehydration to PEN are (i) a low content of alkaline metals (less than 0.5 wt.%), (ii) less than 10 wt.% silica, and (iii) a mean pore diameter between 3 and 15 nm (preferably 4 to 7 nm) and pore volumes preferably between 0.5 and 0.8 cm^3/g. In the experimental conditions used in this work, such parameters are likely not limiting factors. For example, when comparing the pore-size distribution of tested solids in Figure 2B and Table 1 with the kinetic diameters of IPA (0.47 nm), H_2O (0.30 nm) and PEN (0.45 nm) [47,48], it can be concluded that the diffusion of a gaseous mixture of reactive and products is not a determining factor of the activity of different catalysts. This is probably because Mitsui operates under pressure, while we operate near atmospheric pressure.

These findings highlight the importance of specific active acid sites, which could be generated in situ, when steam is present in the reaction mixture (here, IPA produces PEN and H_2O), which correlates with catalytic performances at high conversions and in the absence of textural limiting factors. The determination of acid-base characteristics of fresh powders does not give all relevant information for understanding their catalytic activity in the presence of water. Therefore, the nature, number and strength distribution of acid sites must be considered for aged catalysts (solids in contact with water/steam). It is worth noting that for silica-alumina-like catalysts, characterised by a large variety of acid sites, the adsorption microcalorimetry of probe molecules coupled to manometry is a powerful tool

(among different techniques used to probe acidity of solids such as TPD [49], NMR [50], EPR [51] and FTIR [52]) for quantification and further selection of active sites with defined strengths. Between the methods used to determine the acid/base properties of solid catalysts, based on different chemical and physical principles, adsorption microcalorimetry is the most accurate technique for measuring the differential heats of adsorption and so of characterising a catalyst by the energy distribution of its surface sites [25,53,54]. As demonstrated in this study, determining the number of acid sites with different strengths in solids creates the possibility of finding correlations between the acidity and activity of the catalytic systems.

Comparing the performances of studied catalysts to other investigations is not straightforward because of the different reaction temperatures, contact times and inlet gas compositions used, which are different from those optimised for propylene production, coupled with its further transformation into value-added compounds and at industrial scale.

2.6. Conceptual Process Design

Isopropanol dehydration is better performed under pressure if propylene is the targeted end product [8]. In such a case, the separation of the produced water and remaining isopropanol is facilitated, as propylene is gaseous when other products are liquid.

However, there are a few cases where diluted propylene is a better choice. In the usual selective oxidation of propylene to acrolein, the reaction stream is a mix of propylene, steam, oxygen and nitrogen [55]. The cited reference indicates the current operating conditions: propylene 8–10 mols%, propylene space velocity 150 h^{-1}, pressure 1–1.4 Bar gauge (2–2.4 bars abs) and 300–360 °C. The reaction is highly exothermic and practiced in multitubular reactors, as described in the above reference. To control the reaction, steam is usually added to propylene, and diluted air is necessary to operate outside the flammability limits. A feed composition of propylene/steam/O_2/N_2 in a ratio of 8/8/10.5/73.5 is appropriate. As much water as propylene is commonly used. When isopropanol is dehydrated to propylene, it will also generate as much water. The O_2 content could be reformulated as propylene/steam/air/N_2 = 8/8/47/37, for example. So, isopropanol diluted in nitrogen at about 18 vol % concentration is an appropriate stream to feed a dehydration reactor. The reaction products would be immediately mixed with air and sent to the oxidation reactor. Older acrolein reactions (about four decades ago) used a 5 mol% propylene concentration, so more diluted isopropanol is also possible. However, higher concentrations are limited by the heat released in the selective oxidation reaction and to avoid runaway conditions.

Alternatively, isopropanol can be mixed with diluted air and sent to the dehydration reactor. In the most appropriate configuration, the dehydration reaction has to be sufficiently fast so that the contact time required would be a fraction of the contact time needed for the oxidation reaction. The reactor is still the conventional multitubular reactor, but on top of the oxidation catalyst, a thin layer of dehydration catalyst is added. With such a design, the capital cost in an existing unit is minimised, as it is not necessary to replace the expensive multitubular reactor, and the downstream purification unit would remain identical (provided that no new impurities is generated). To simplify a contact time for the dehydration reaction in the range of 0.2–0.4 s is required with a temperature of the catalyst layer at the entrance of the reactor between 200 and 300 °C.

When no catalyst working in such conditions can be found, then a separate reactor for the dehydration reaction is needed with the appropriate residence time and temperature. It operates either in the presence of oxygen or not. The dehydration reaction being endothermic, it benefits from the heat generated by the oxidation reaction, and could be heated either by the molten salt or by the steam produced by the boiler while cooling the salt.

For such an application, it is needed to develop a catalyst working near atmospheric pressure, at a temperature between 200 and 300 °C, eventually in the presence of oxygen. It must operate at very high conversion, as isopropanol would be oxidised to acetone and/or acetic acid in the oxidation reactor, and it must not generate side products that would compromise the acrolein quality. Some acetone and acetaldehyde are possible, as they are already impurities produced in the selective oxidation reaction. Trace amounts of formaldehyde are also possible, as well as a very low concentration of propanaldehyde. It is unexpected to be produced in the dehydration reaction; however, n-propanol could be produced by dehydration–rehydration of propylene. N-propanol is expected to lead to n-propanaldehyde in the selective oxidation reaction. Therefore, it is very important to identify the operating conditions and catalysts that minimise the formation of n-propanol from isopropanol.

3. Materials and Methods

3.1. Catalysts

The studied materials were commercial solids as follows: two alumina powders from BASF (Ludwigshaffen, Germany) and Grace Davison (Columbia, MD, USA), SiO_2-Al_2O_3 solids with Si/Al ratios of 5, 30, and 75 from Sasol Germany GmbH (Brunsbüttel, Germany) and SiO_2 from Grace Davison. The silica–alumina composites were denoted as a function of $SiO_2/(SiO_2+Al_2O_3)$ ratio as 5-SiO_2-Al_2O_3, 30-SiO_2-Al_2O_3 and 75-SiO_2-Al_2O_3 for ratios of 5, 30, and 75, respectively, given by the supplier. These values were confirmed by X-ray fluorescence spectrometry (XRF), except for 75-SiO_2-Al_2O_3, for which the $SiO_2/(SiO_2+Al_2O_3)$ ratio was found to be 79.5%. In XRF measurements, the instrumental relative errors below 10% were identified by Li et al. [56]. Nieminen and Niinistö [57] found relative standard deviations between 0.2 and 4% when Al/Si ratio was determined by XRF.

The as-received materials were hydrothermally treated in hot water at 100 °C in order to investigate the water-ageing impact on their textural and chemical properties.

The tests were performed by using a slurry of the sample (1 g) in deionised water (10 mL) in a reflux setup at 100 °C for 2 h under vigorous stirring. The treated samples were further filtered and dried at 100 °C overnight. The obtained materials are denoted as water-aged samples and were stored in a closed container in the laboratory atmosphere. XRF analysis were performed after storage for several months, and no significant difference in the $SiO_2/(SiO_2+Al_2O_3)$ ratios was detected. A value of 76% was determined for $SiO_2/(SiO_2+Al_2O_3)$ ratio in the high-loaded water-aged silica sample. Although this result could be considered below the known errors of the technique, some leaching of silicon cannot be completely excluded.

3.2. Catalyst Characterisation

3.2.1. X-Ray Diffraction (XRD)

The XRD patterns of all the samples were recorded on a Brüker D8 Advance powder diffractometer, with monochromatic Cu Kα radiation of 1.5406 Å wavelength, equipped with a 1-D fast multistrip detector (LynxEye, 192 channels, 2.95°) and a Ni filter. The diffractograms, registered within the 2θ range from 4 to 80° with a 0.02° step size, were analysed using Diffract Eva software and the PDF4+ database.

3.2.2. Nitrogen Sorption

Nitrogen sorption isotherms were recorded at −196 °C on an ASAP 2010 (Micromeritics) apparatus. The samples were first outgassed under secondary vacuum for 3 h at 300 °C. The apparent specific surface areas (S_{BET}) were derived from the BET (Brunauer–Emmett–Teller) standard equation. The interval of relative pressure used to linearise the

BET model equation was $0.005 \leq P/P_0 \leq 0.10$ with at least 5 points, used to obtain a correlation coefficient > 0.999. The total pore volume (V_{porous}) was calculated at $P/P_0 = 0.98$ on the adsorption branch. The mesopore-size distribution was determined by analysing the desorption branch of the N_2 isotherm (BJH method).

3.2.3. Adsorption Microcalorimetry

The acid/base properties of the catalysts were determined at 150 °C by adsorption microcalorimetry of NH_3 and SO_2 probe molecules. A complete description of the technique used and its specific principle is given in [58]. Each fresh sample (around 0.100 g) was thermally treated in the quartz calorimetric cell overnight at 400 °C under vacuum (10^{-5} Pa) prior to adsorption experiment. The heats of adsorption were measured in a heat-flow microcalorimeter of the Tian–Calvet type (C80 from Setaram, France) linked to a volumetric line equipped with a Barocel capacitance manometer (Datametrics) for pressure measurements. The adsorption experiment consisted in repeatedly sending small doses of gas (NH_3 or SO_2) onto the outgassed solid while recording concomitantly the heat flow signal and the pressure evolution. Both calorimetric and volumetric data were stored and analysed by microcomputer processing. The adsorption run, carried out until a final equilibrium pressure of 67 Pa, was followed by powder outgassing under vacuum for approximately 40 min. After evacuation, a second run of adsorption was performed until attaining an equilibrium pressure of 27 Pa. The adsorption isotherms correlate the amount of probe molecules adsorbed with the corresponding equilibrium pressure. The first adsorption allows measuring the overall uptake of probe gas (n_{tot}) on the catalyst. By subtracting the second isotherm from the first one, the irreversibly adsorbed amount (n_{irr}) of probe gas was obtained. An estimation of the number of strong acidic and basic sites can be derived from n_{irr} (often associated with adsorption heats at least of the order of 100–150 kJ/mol, depending on the probe molecule and the experimental conditions). Further, the variation of the differential heats of adsorption with coverage gave access to energy distribution of surface-active sites with respect to a given adsorbate and their varying reactivity on given adsorbents.

3.2.4. Nuclear Magnetic Resonance (NMR)

The NMR spectra were obtained on a Bruker AVANCE III 500WB NMR spectrometer. ^{29}Si experiments were performed under HPDEC (high-power decoupling−magic angle spinning with ^{1}H decoupling) conditions at 99.34 MHz. The following NMR parameters were used: proton pulse width of 4 µs, a 10 kHz rotor spinning rate and 4 mm double H/X probe. The chemical shifts are reported in parts per million (ppm) relative to Q8M8 (12.4 pm). For ^{27}Al experiments, the reference used for measuring the chemical shift was a solution of $Al(NO_3)_3$ 1M. The spectra were recorded under MAS conditions (magic angle spinning without ^{1}H decoupling) at 130.29 MHz with a rotor spinning rate of 12 kHz, 0.5 µs pulse and a triple 4 mm H/X/Y probe.

3.2.5. FTIR Studies

All IR spectra were recorded at room temperature at a resolution of 4 cm^{-1} in the region of 400−4000 cm^{-1} by using a Thermo Scientific (Waltham, MA, USA) Nicolet 8700 Fourier transform spectrometer equipped with a DTGS detector and OMNIC software.

Various surface species were analysed for fresh and water-aged powders. Prior to analysis, 1 mg of sample was mixed with 100 mg of KBr (spectroscopy grade; Sigma-Aldrich (Saint-Quentin-Fallavier, France); stored at 110 °C in an oven). The mixture was finely ground in an agate mortar and pressed into pellets of less than 3 tons/cm^2.

For NH_3 adsorption/desorption FTIR study, the samples were pressed into self-supporting discs of about 40 mg. The self-supported wafer was placed into a cell with

CaF_2 windows and activated under oxygen overnight at 400 °C (1 °C/min), followed by 2 h outgassing at the same temperature before adsorption. Then, the cell was cooled down to 25 °C, and the sample was contacted with NH_3 (15 mbars) for 1 h before following the desorption of the adsorbed species, under vacuum, at 25, 100, 200, 300 and 400 °C. The IR spectra were recorded after each step: activation, adsorption and desorption at different temperatures.

3.3. Catalytic Test

Isopropanol was purchased from Carlo Erba Reagents (Val-de-Reuil, France) and was used for the catalytic reaction without further purification. (Only the absence of peroxides was regularly checked). Helium gas (N5.0 purity) was supplied by Messer. The catalytic conversion of IPA was performed in a tubular U-shaped reactor in stainless steel with an inner diameter of 4.57 mm at atmospheric pressure, temperatures between 200 and 300 °C and 0.2 s residence time. The reactor was first packed with a layer of glass wool at the bottom to provide support, and then the catalyst (about 0.1 mL, 180–300 µm particle size) was loaded between two layers of ≈ 0.1 mL of silicon carbide (106–150 µm). The upper empty volume of the reactor was filled with the SiC (840–1150 µm), which helped heat the reactive mixture to the reaction temperature. Glass wool was added to the topmost layer of the reactor outlet to prevent potential migration of the SiC to the column channel. The post-reaction space in the reactor was reduced by using a small-diameter (1/8) tube to avoid further conversion of the products in the gas phase. Figure 10 presents the catalytic test setup, the reactor characteristics and the disposition of the catalyst inside the reactor. The temperature in the reactor was controlled by a Eurotherm controller using a K-type thermocouple placed in the middle of the catalyst bed. Prior to the catalytic tests, the samples were treated in situ in He flow (30 mL_{NTP}/min) at 300 °C for 1.5 h. The reactor was cooled down to the desired reaction temperature and the catalytic performances measured in a temperature rising sequence. The isopropanol was supplied by passing He carrier gas (28.5 mL_{NTP}/min, controlled by a calibrated mass flow controller) through a saturator holding the alcohol at 23 °C (Julabo bath) for a constant partial pressure of IPA of 5136 Pa. An IPA/He mixture of 5 vol% was fed through the top of the reactor at total feed rate of 30 mL_{NTP}/min. The inlet and outlet gas lines of the reactor were kept at 140 °C by heating tapes in order to avoid the condensation of reactant and products. The IPA reactant and products (propylene, acetone, H_2O and di-isopropyl ether) were analysed by sampling 100 µL of gases in a Perkin Elmer gas chromatograph equipped with a stainless-steel Porapak Q packed column (80/100 mesh, ϕ 3 m × 2.1 mm), and both a flame ionisation (FID) and a thermal conductivity (TCD) detector. Helium was used as carrier gas in the GC. The GC response factor was calibrated using various compositions of IPA, ACE and PEN.

The mean absolute percentage error in alcohol conversion was ≤ 5%, and the carbon balance was maintained within 95%. The carbon balance was defined as the fraction of all the carbon atoms recovered at the reactor outlet (PEN, ACE, and IPA) over all carbon atoms fed into the reactor (IPA).

The performances of studied materials were compared after 2 h from the initial introduction of the reactant into the reactor when the reaction equilibrium steady-state conditions were attained for the catalytic reaction. The conversion of IPA was calculated as the ratios (%) of the total products to the IPA introduced. The selectivities were calculated as the ratio (%) of the product yield to the conversion of IPA.

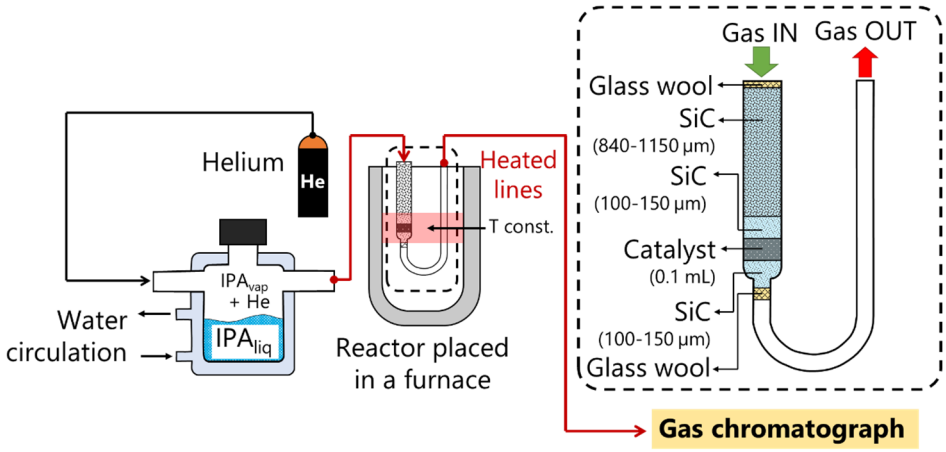

Figure 10. Schematic diagram of the catalytic testing setup with an overview on the reactor filling.

Prior to the catalytic tests, control experiments were performed in an empty reactor and over a SiC-filled reactor under the same reaction conditions. The background IPA conversion was negligible.

It is important to mention that (i) a steady state was reached very quickly after each temperature change for all tested solids, (ii) the initial conversion was fully recovered when the temperature was decreased back to 250 °C after testing at 300 °C, and (iii) no deactivation was observed in the experimental conditions used.

4. Conclusions

The catalytic properties of commercial alumina and silica–alumina with different SiO_2 contents in the isopropanol dehydration-featuring operation conditions (5 mol% IPA, 0.2 s contact time, 200–300 °C, atmospheric pressure) for further selective oxidation of produced propylene to acrolein were studied. At 300 °C, all catalysts achieved complete conversion, with propylene being the main product together with traces of acetone. The selectivity towards PEN was 100% at 200 °C. At this temperature, it is believed that sites responsible for the catalytic activity are strong acid sites (>150 kJ/mol, as determined by adsorption microcalorimetry of NH_3 adsorption at 150 °C). NH_3-FTIR spectroscopy revealed the presence of mostly Lewis acidity between 200 and 300 °C, which could be partly hydrated under catalytic testing, water being one of the products of dehydration reaction. For SiO_2-Al_2O_3 samples, the hydrothermal treatment induced the generation of new acid site of medium-high strengths, while the redistribution of acid sites strength was observed for pure alumina solids. A linear relationship between the amount of the strong acid sites in the water-aged catalysts and the IPA conversion was found, indicating that the complete description of acidic properties on solid surfaces requires their determination for both fresh and water-contacted powders. Between silica-alumina samples, 30-SiO_2-Al_2O_3 preserved its textural properties during hydrothermal treatment. Its high stability and good catalytic performances, together with its commercial availability and low cost, make 30-SiO_2-Al_2O_3 a potential candidate for use as catalyst layer at the entrance of the oxidation reactor for acrolein production. The scale-up of such a process provides a new opportunity for implementation of bio-based alcohols for acrolein production.

Author Contributions: Conceptualisation, G.P., A.A. and J.-L.D.; methodology, G.P. and J.-L.D.; investigation, S.S., T.C. and T.-H.N.; resources, G.P.; data curation, S.S., T.C. and T.-H.N.; writing—original draft preparation, G.P. and J.-L.D.; writing—review and editing, G.P., A.A. and J.-L.D.; supervision, G.P.; project administration, G.P. All authors have read and agreed to the published version of the manuscript.

Funding: This project has received funding from the European Union's Horizon 2020 research and innovation programme under grant agreement No. 101037009.

Data Availability Statement: The original contributions to the study are included in the article.

Acknowledgments: The authors acknowledge the scientific services of IRCELYON (IRC@TECH characterisation platform). G.P. thanks P. Gélin for fruitful discussions.

Conflicts of Interest: Author Jean-Luc DUBOIS is employed by the company Trinseo. The remaining authors declare that the research was conducted in the absence of any commercial or financial relationships that could be construed as a potential conflict of interest.

Abbreviations

The following abbreviations are used in this manuscript:

IPA	isopropanol
PEN	propylene
ACE	acetone

References

1. Blay, V.; Epelde, E.; Miravalles, R.; Alvarado Perea, L. Converting olefins to propene: Ethene to propene and olefin cracking. *Catal. Rev.* **2018**, *60*, 278–335. [CrossRef]
2. Phung, T.K.; Le Minh Pham, T.; Vu, K.B.; Busca, G. (Bio)Propylene production processes: A critical review. *J. Environ. Chem. Eng.* **2021**, *9*, 105673. [CrossRef]
3. Shirzad, P.; Kantor, I. Toward sustainable propylene: A comparison of current and future production pathways. *Renew. Sustain. Energy Transit.* **2025**, *7*, 100099. [CrossRef]
4. Propylene Market Size, Share, and Trends 2025 to 2034. Precedence Research. 2025. Available online: https://www.precedenceresearch.com/propylene-market (accessed on 10 June 2025).
5. Propylene Market Size, Share & Industry Analysis, By Derivative, By Application, and Regional Forecast, 2024−2032. Fortune Business Insights. 2025. Available online: https://www.fortunebusinessinsights.com/propylene-market-109718 (accessed on 10 June 2025).
6. Oil 2025 Analysis and Forecast 2030. International Energy Agency. 2025. Available online: https://iea.blob.core.windows.net/assets/018c3361-bc01-4482-a386-a5b2747ae82a/Oil2025.pdf (accessed on 27 June 2025).
7. Global propylene demand and capacity 2015 to 2022. Statista. 2025. Available online: https://www.statista.com/statistics/1246689/propylene-demand-capacity-forecast-worldwide/ (accessed on 27 June 2025).
8. Dubois, J.-L.; Postole, G.; Silvester, L.; Auroux, A. Catalytic Dehydration of Isopropanol to Propylene. *Catalysts* **2022**, *12*, 1097. [CrossRef]
9. Polo-Garzon, F.; Yang, S.Z.; Fung, V.; Foo, G.S.; Bickel, E.E.; Chisholm, M.F.; Jiang, D.E.; Wu, Z. Controlling reaction selectivity through the surface termination of perovskite catalysts. *Angew. Chem. Int. Ed. Engl.* **2017**, *56*, 9820–9824. [CrossRef]
10. Bao, Z.; Fung, V.; Polo-Garzon, F.; Hood, Z.D.; Cao, S.; Chi, M.; Bai, L.; Jiang, D.; Wu, Z. The interplay between surface facet and reconstruction on isopropanol conversion over $SrTiO_3$ nanocrystals. *J. Catal.* **2020**, *384*, 49–60. [CrossRef]
11. Bautista, F.M.; Campelo, J.M.; García, A.; Luna, D.; Marinas, J.M.; Romero, A.A.; Siles, M.T. Vanadyl–aluminum binary phosphate: Al/V ratio influence on their structure and catalytic behavior in the 2-propanol conversion. *Catal. Today* **2003**, *78*, 269–280. [CrossRef]
12. Gervasini, A.; Fenyvesi, J.; Auroux, A. Study of the acidic character of modified metal oxide surfaces using the test of isopropanol decomposition. *Catal. Lett.* **1997**, *43*, 219–228. [CrossRef]
13. Larmier, K.; Chizallet, C.; Maury, S.; Cadran, N.; Abboud, J.; Lamic-Humblot, A.-F.; Marceau, E.; Lauron-Pernot, H. Isopropanol Dehydration on Amorphous Silica–Alumina: Synergy of Brønsted and Lewis Acidities at Pseudo-Bridging Silanols. *Angew. Chem. Int. Ed.* **2017**, *56*, 230–234. [CrossRef]
14. Turek, W.; Haber, J.; Krowiak, A. Dehydration of isopropyl alcohol used as an indicator of the type and strength of catalyst acid centres. *Appl. Surf. Sci.* **2005**, *252*, 823–827. [CrossRef]
15. Ouqour, A.; Coudurier, G.; Vedrine, J.C. Acid–base properties of metallic oxide catalysts studied by conversion of propan-2-ol. *J. Chem. Soc. Faraday Trans.* **1993**, *89*, 3151–3155. [CrossRef]
16. Panjapakkul, W.; El-Halwag, M.M. Technoeconomic Analysis of Alternative Pathways of Isopropanol Production. *ACS Sustainable Chem. Eng.* **2018**, *6*, 10260–10272. [CrossRef]

17. Folliard, V.; de Tommaso, J.; Dubois, J.-L. Review on Alternative Route to Acrolein through Oxidative Coupling of Alcohols. *Catalysts* **2021**, *11*, 229. [CrossRef]
18. Stuart, N.M.; Sohlberg, K. The Microstructure of γ-Alumina. *Energies* **2021**, *14*, 6472. [CrossRef]
19. Sarker, S.R.; Alam, Z.; Qadir, R.; Gafur, M.A.; Moniruzzaman, M. Extraction and characterization of alumina nanopowders from aluminum dross by acid dissolution process. *Int. J. Miner. Metall. Mater.* **2015**, *22*, 429. [CrossRef]
20. Cai, S.-H.; Rashkeev, S.N.; Pantelides, S.T.; Sohlberg, K. Phase transformation mechanism between γ- and θ-alumina. *Physical Review B* **2003**, *67*, 224104. [CrossRef]
21. Sing, S.W.; Everett, D.H.; Haul, R.A.W.; Moscou, L.; Pierotti, R.A.; Rouquerol, J.; Siemieniewska, T. Reporting physisorption data for gas/solid systems—With special reference to the determination of surface area and porosity. *Pure Appl. Chem.* **1985**, *57*, 603. [CrossRef]
22. Thommes, M. Physical Adsorption Characterization of Nanoporous Materials. *Chemie Ingenieur Technik* **2010**, *82*, 1059. [CrossRef]
23. Sarkar, A.; Gupta, N.; Biswas, S.K. Bimodal mesoporous α-Fe_2O_3/SiO_2 composite: A highly efficient heterogeneous solar-driven photo-Fenton catalyst. *J. Molec. Structure* **2023**, *1284*, 135373. [CrossRef]
24. Hahn, M.W.; Copeland, J.R.; van Pelt, A.H.; Sievers, C. Stability of Amorphous Silica–Alumina in Hot Liquid Water. *ChemSusChem* **2013**, *6*, 2304–2315. [CrossRef]
25. Auroux, A.; Védrine, J.C. *Catalysis by Acids and Bases*; Imelik, B., Naccache, C., Coudurier, G., Taarit, Y.B., Vedrine, J.C., Eds.; Studies in Surface Science and Catalysis 20; Elsevier: Amsterdam, The Netherlands, 1985; p. 311.
26. Thomas, J.M.; Klinowski, J. The Study of Aluminosilicate and Related Catalysts by High Resolution Solid-State NMR Spectroscopy. *Adv. Catal.* **1985**, *33*, 199.
27. McMillan, M.; Brinen, J.S.; Carruthers, J.D.; Haller, G.L. A ^{29}Si NMR Investigation of the Structure of Amorphous Silica-Alumina Supports. *Colloids Surf.* **1989**, *38*, 133–148. [CrossRef]
28. Knözinger, H.; Ratnasamy, P. Catalytic Aluminas: Surface Models and Characterization of Surface Sites. *Catal. Rev. Sci. Eng.* **1978**, *17*, 31–70. [CrossRef]
29. Mägi, M.; Lippmaa, E.; Samoson, A.; Engelhardt, G.; Grimmer, A.-R. Solid-State High-Resolution Silicon-29 Chemical Shifts in Silicates. *J. Phys. Chem.* **1984**, *88*, 1518–1522. [CrossRef]
30. Man, P.P.; Peltre, M.J.; Barthomeuf, D. Nuclear Magnetic Resonance Study of the Dealumination of an Amorphous Silica-Alumina Catalyst. *J. Chem. Soc. Faraday Trans.* **1990**, *86*, 1599–1602. [CrossRef]
31. Dorémieux-Morin, C.; Martin, C.; Brégeault, J.-M.; Fraissard, J. Multinuclear high-resolution solid-state nuclear magnetic resonance studies of amorphous silica-aluminas. *Appl. Catal.* **1991**, *77*, 149–161. [CrossRef]
32. Dorémieux-Morin, C.; Batamack, P.; Martin, C.; Brégeault, J.-M.; Fraissard, J. Comparison of amorphous silica-alumina and highly dealuminated HY zeolite by ^{1}H high resolution MAS-NMR of solides. *Catal. Lett.* **1991**, *9*, 403–410. [CrossRef]
33. Busca, G.; Lorenzelli, V.; Ramis, G.; Willey, R.J. Surface Sites on Spinel-Type and Corundum-Type Metal Oxide Powders. *Langmuir* **1993**, *9*, 1492–1499. [CrossRef]
34. Tarte, P. Infra-red spectra of inorganic aluminates and characteristic vibrational frequencies of AlO_4 tetrahedra and AlO_6 octahedra. *Spectrochim. Acta A* **1967**, *23*, 2127–2143. [CrossRef]
35. Finocchio, E.; Busca, G.; Rossini, S.; Cornaro, U.; Piccoli, V.; Miglio, R. FT-IR characterization of silicated aluminas, active olefin skeletal isomerization catalysts. *Catal. Today* **1997**, *33*, 335–352. [CrossRef]
36. Morterra, C.; Mognacca, G. A case study: Surface chemistry and surface structure of catalytic aluminas, as studied by vibrational spectroscopy of adsorbed species. *Catal. Today* **1996**, *27*, 497–532. [CrossRef]
37. Ellerbrock, R.; Stein, M.; Schaller, J. Comparing amorphous silica, short-range-ordered silicates and silicic acid species by FTIR. *Sci. Rep.* **2022**, *12*, 11708. [CrossRef] [PubMed]
38. Busca, G. Silica-alumina catalytic materials: A critical review. *Catal. Today* **2020**, *357*, 621–629. [CrossRef]
39. Busca, G. Catalytic materials based on silica and alumina: Structural features and generation of surface acidit. *Prog. Mater. Sci.* **2019**, *104*, 215–249. [CrossRef]
40. Tsyganenko, A.A.; Pozdnyakov, D.V.; Filimonov, V.N. Infrared study of surface species arising from ammonia adsorption on oxide surfaces. *J. Molec. Struct.* **1975**, *29*, 299–318. [CrossRef]
41. Lavalley, J.C.; Benaissa, M. Infrared study of surface modes on alumina. Elsevier, Eds: M. Che, G.C. Bond. *Stud. Surf. Sci. Catal.* **1985**, *21*, 251–261.
42. Mapes, J.E.; Eischens, R.P. The infrared spectra of ammonia chemisorbed on cracking catalysts. *J. Phys. Chem.* **1954**, *58*, 1059–1062. [CrossRef]
43. Li, M.; Shen, J. Microcalorimetric Adsorption Characterizations of Supported Vanadia Catalysts for the Selective Oxidation of Propylene to Acetone. *J. Catal.* **2002**, *205*, 248–258. [CrossRef]
44. Chizallet, C.; Raybaud, P. Pseudo-Bridging Silanols as Versatile Brønsted Acid Sites of Amorphous Aluminosilicate Surfaces. *Angew. Chem.* **2009**, *121*, 2935–2937. [CrossRef]
45. Busca, G. The surface of transitional aluminas: A critical review. *Catal. Today* **2014**, *226*, 2–13. [CrossRef]

46. Fukuhara, H.; Matsunaga, F.; Yasuhara, M.; Araki, S.; Isaka, T. Preparation of Propylene. European Patent EP0379803, 30 December 1989. Assigned to MITSUI Petrochemical Industries Ltd. Available online: https://worldwide.espacenet.com/patent/search/family/026547935/publication/EP0379803A1?q=EP0379803 (accessed on 10 August 2022).
47. van Leeuwen, M.E. Derivation of Stockmayer potential parameters for poral fluids. *Fluid Phase Equilibria* **1994**, *99*, 1–18. [CrossRef]
48. Perez, E.V.; Karunaweera, C.; Musselman, I.H.; Balkus, K.J., Jr.; Ferraris, J.P. Origins and Evolution of Inorganic-Based and MOF-Based Mixed-Matrix Membranes for Gas Separations. *Processes* **2016**, *4*, 32. [CrossRef]
49. Arena, F.; Dario, R.; Parmalian, A. A characterization study of the surface acidity of solid catalysts by temperature programmed methods. *Appl. Catal. A Gen.* **1998**, *170*, 127–137. [CrossRef]
50. Peng, Y.-K.; Tsang, S.-C.E. Probe-assisted NMR: Recent progress on the surface study of crystalline metal oxides with various terminated facets. *Magn. Reson. Lett.* **2022**, *2*, 9–16. [CrossRef]
51. Chuklina, S.; Zhukova, A.; Fionov, Y.; Kadyko, M.; Fionov, A.; Zhukov, D.; Ilícheva, A.; Podzorova, L.; Mikhalenko, I. Selectivity of Ethanol Conversion on Al/Zr/Ce Mixed Oxides: Dehydration and Dehydrogenation Pathways Based on Surface Acidity Properties. *ChemistrySelect* **2022**, *7*, e202203031. [CrossRef]
52. Barzetti, T.; Selli, E.; Moscotti, D.; Forni, L. Pyridine and ammonia as probes for FTIR analysis of solid acid catalysts. *J. Chem. Soc. Faraday Trans.* **1996**, *92*, 1401–1407. [CrossRef]
53. Auroux, A. Acidity characterization by microcalorimetry and relationship with reactivity. *Top. Catal.* **1997**, *4*, 71–89. [CrossRef]
54. Mishin, I.V.; Brueva, T.R.; Kapustin, G.I. Heats of adsorption of ammonia and correlation of activity and acidity in heterogeneous catalysis. *Adsorption* **2005**, *11*, 415–424. [CrossRef]
55. Available online: https://www.man-es.com/docs/default-source/document-sync/salt_operated_reactors_acrolein.pdf?sfvrsn=71a54ff3_7 (accessed on 10 June 2025).
56. Li, G.; Klein, B.; Sun, C.; Kou, J. Lab-scale error analysis on X-ray fluorescence sensing for bulk ore sorting. *Miner. Eng.* **2021**, *164*, 106812. [CrossRef]
57. Nieminen, M.; Niinistö, L. Determination of aluminium in $AlCl_3$ and Al_2O_3 modified silica catalyst supports. *Fresenius J. Anal. Chem.* **1999**, *364*, 224–227. [CrossRef]
58. Auroux, A. *Catalysts Characterization: Physical Techniques for Solid Materials*; Imelik, B., Vedrine, J.C., Eds.; Plenum Press: New York, NY, USA, 1994; p. 611.